



HAL
open science

Terahertz near-field imaging of surface plasmon waves in graphene structures

O. Mitrofanov, W. Yu, R J Thompson, Yuchao Jiang, Z. J Greenberg, J. Palmer, I. Brener, W. Pan, Claire Berger, W.A. de Heer, et al.

► To cite this version:

O. Mitrofanov, W. Yu, R J Thompson, Yuchao Jiang, Z. J Greenberg, et al.. Terahertz near-field imaging of surface plasmon waves in graphene structures. *Solid State Communications*, 2015, 224, pp.47 - 52. 10.1016/j.ssc.2015.08.013 . hal-01784084

HAL Id: hal-01784084

<https://hal.science/hal-01784084>

Submitted on 3 May 2018

HAL is a multi-disciplinary open access archive for the deposit and dissemination of scientific research documents, whether they are published or not. The documents may come from teaching and research institutions in France or abroad, or from public or private research centers.

L'archive ouverte pluridisciplinaire **HAL**, est destinée au dépôt et à la diffusion de documents scientifiques de niveau recherche, publiés ou non, émanant des établissements d'enseignement et de recherche français ou étrangers, des laboratoires publics ou privés.

Terahertz near-field imaging of surface plasmon waves in graphene structures

O. Mitrofanov^{a,b,*}, W. Yu^c, R. J. Thompson^a, Y. Jiang^c, Z. J. Greenberg^c, J. Palmer^c
I. Brener^{b,d}, W. Pan^d, C. Berger^{c,e}, W. A. de Heer^c, Z. Jiang^{c,**}

^a Electronic and Electrical Engineering, University College London, London WC1E 7JE, United Kingdom

^b Center for Integrated Nanotechnologies, Sandia National Laboratories, Albuquerque, New Mexico 87185, U.S.A.

^c School of Physics, Georgia Institute of Technology, Atlanta, Georgia 30332, U.S.A.

^d Sandia National Laboratories, Albuquerque, New Mexico 87185, U.S.A.

^e CNRS/Institut Néel, BP166, 38042 Grenoble, France

ABSTRACT

We introduce a near-field scanning probe terahertz (THz) microscopy technique for probing surface plasmon waves on graphene. Based on THz time-domain spectroscopy method, this near-field imaging approach is well suited for studying the excitation and evolution of THz plasmon waves on graphene as well as for mapping of graphene properties at THz frequencies on the sub-wavelength scale.

Keywords: E. THz near-field microscopy; D. Surface plasmons; A. Epitaxial graphene.

1. Introduction

Graphene plasmons, the collective oscillations of Dirac fermions enabling strong enhancement of light-matter interaction, have recently attracted a great deal of attention (for a recent review, see Ref. [1]). It has been shown that surface plasmons can be confined in graphene nanostructures with a characteristic dimension more than 100 times smaller than the wavelength of incident light [2, 3]. Graphene plasmons are highly tunable; the plasmon frequency depends on the carrier density and doping [4-6], the characteristic dimension (for graphene structures) [4, 5, 7], the number of stacked layers [5], the packing density of graphene structures [8], the substrate phonon modes [9, 10], and the applied magnetic field [3, 7, 11]. Graphene plasmons can be excited and probed locally using a scattering-type scanning near-field optical microscope with a focused infrared beam [12, 13]. Such a high-resolution near-field technique has created great excitement in the field. The spectral range of these studies ($600\text{-}2500\text{ cm}^{-1}$) was however limited by the mid-infrared light source [14].

In the terahertz (THz) spectral range ($10\text{-}100\text{ cm}^{-1}$) graphene also exhibits rich physics and great application potential [15-17]. THz spectroscopy and imaging techniques have been used to study the THz conductivity of graphene [18-20], enabling non-contact characterization of graphene and providing direct information about its doping level and uniformity. These far-field methods however provide only limited information about plasmon excitations, which are localized at the surface. In this Communication, we will introduce a near-field scanning probe THz microscopy technique for probing graphene plasmons at THz frequencies. Based on time-domain analysis, this technique is particularly suited for studies of excitation and propagation of surface waves [21].

2. Material and methods

2.1. Epitaxial graphene on silicon carbide

* Corresponding author. Tel: (O.M.)+44 (0)20 76793128.

** Corresponding author. Tel: (Z.J.)+1 4043853906.

E-mail addresses: o.mitrofanov@ucl.ac.uk (O.M.), zhigang.jiang@physics.gatech.edu (Z.J.).

The epitaxial graphene studied in this work was grown on silicon carbide (SiC) substrate using a diffusion-limited confinement controlled sublimation method [22]. Generally speaking, there are two principally different types of epitaxial graphene forming on the Si- or C-terminated face of SiC, respectively. The growth on the Si-terminated face has a better layer control and the material consists of mono- and bi-layers of graphene but with a relatively high carrier concentration due to the charge transfer from SiC [23]. The graphene grown on the C-terminated face however are usually multilayers. Although the first few layers of graphene close to the interface with SiC are still highly doped (as that on the Si-terminated face), the subsequent top layers are practically charge neutral and electrically decoupled from each other behaving like monolayer graphene [24, 25]. The Fermi energy of such quasi-neutral top layers of graphene is typically $E_F < 20$ meV [3, 25], while $E_F > 200$ meV for the highly doped layers close to the interface [23].

The epitaxial graphene samples were patterned into mesas and ribbon arrays via standard electron-beam lithography, followed by oxygen plasma etching and high vacuum annealing. The vacuum annealing process is crucial for removing the chemical residue left on graphene surface after lithography. The annealing was conducted in high vacuum ($< 5 \times 10^{-5}$ mTorr) at 600 °C for 2 hours. Cyclotron resonance measurements reveal that the vacuum annealed top graphene layers grown on the C-terminated face recover their low density and high mobility, $E_F \approx 17$ meV and $\mu > 50,000$ cm²V⁻¹s⁻¹ [3], similar to the values observed in as-grown samples.

2.2. THz near-field microscopy and its application on metallic surfaces

Graphene ribbon arrays allow excitation of confined plasmon modes by a plane wave incident at normal incidence [4, 9], similar to periodic metallic structures (arrays of ribbons or corrugations). Even a continuous graphene mesa can in principle support surface plasmon waves. In the latter case, the surface wave can be excited at the mesa edges, similar to the excitation of surface waves at the edges of metallic patterns [26, 27]. Unlike the metallic films however, graphene is highly transparent to the incident electromagnetic wave. The transmission coefficient for a graphene layer at THz frequencies can be reduced only to the level of 60-70%, even for the highest achievable carrier densities [18-21]. This presents a challenge for observation and investigations of surface plasmon waves in graphene structures: the incident THz wave is typically dominant in the region where the confined plasmon modes and surface plasmon waves are excited.

Studies of surface plasmons in graphene therefore require both local (near-field) probing at the surface and method for differentiating surface plasmon waves from the incident wave. In this work, we will address the questions of excitation and detection of THz surface plasmon waves on patterned graphene structures illuminated by a plane incident wave. In our analysis of THz surface waves, we take advantage of the temporal resolution provided by the THz time-domain spectroscopy technique. Combined with near-field scanning probe THz microscopy [27], this method allows detecting temporal evolution of the electric field distribution over the surface, in which surface wave signatures become apparent.

The near-field probe employed in this study is an integrated sub-wavelength aperture probe. It detects THz waves through a 10 μ m input aperture [28]. For excitation, we use short THz pulses (~ 2 ps) with the spectrum covering the frequency range from 0.5 to 2.5 THz. Before discussing THz surface plasmon waves on graphene, we briefly examine THz surface plasmon signatures on metallic surfaces.

Consider a metallic pattern, for example a bow-tie antenna, on a dielectric substrate illuminated by a plane wave at normal incidence from the substrate side. Such an experimental configuration is illustrated in Fig. 1(a). We use a large diameter THz waveguide with a well-defined beam profile for illumination of the antenna. The waveguide also ensures that the incident wave is described by a narrow distribution of wave-vectors ($|k_x| < 0.1 k_z$) centered around $k_x = 0$.

The incident THz wave induces charges at the edges of the bow-tie antenna. The electric field distribution near the antenna as a result has regions of field concentration near the edges, where the field component perpendicular to the surface, E_z is created in addition to the E_x -component of the incident field (Fig. 1(b)). The E_z -component starts propagating away from the edge as a surface wave [27, 29].

To understand how the incident THz wave with $k_x = 0$ couples into the surface wave, it is useful to consider the angular spectrum representation of the induced E_z -component near the edge. This field is localized at the edge and thus it contains a broad distribution of wave-vectors k_x (as illustrated in the upper panel of Fig. 1(b)). For any frequency of the incident wave ω_0 , there is a component in the angular

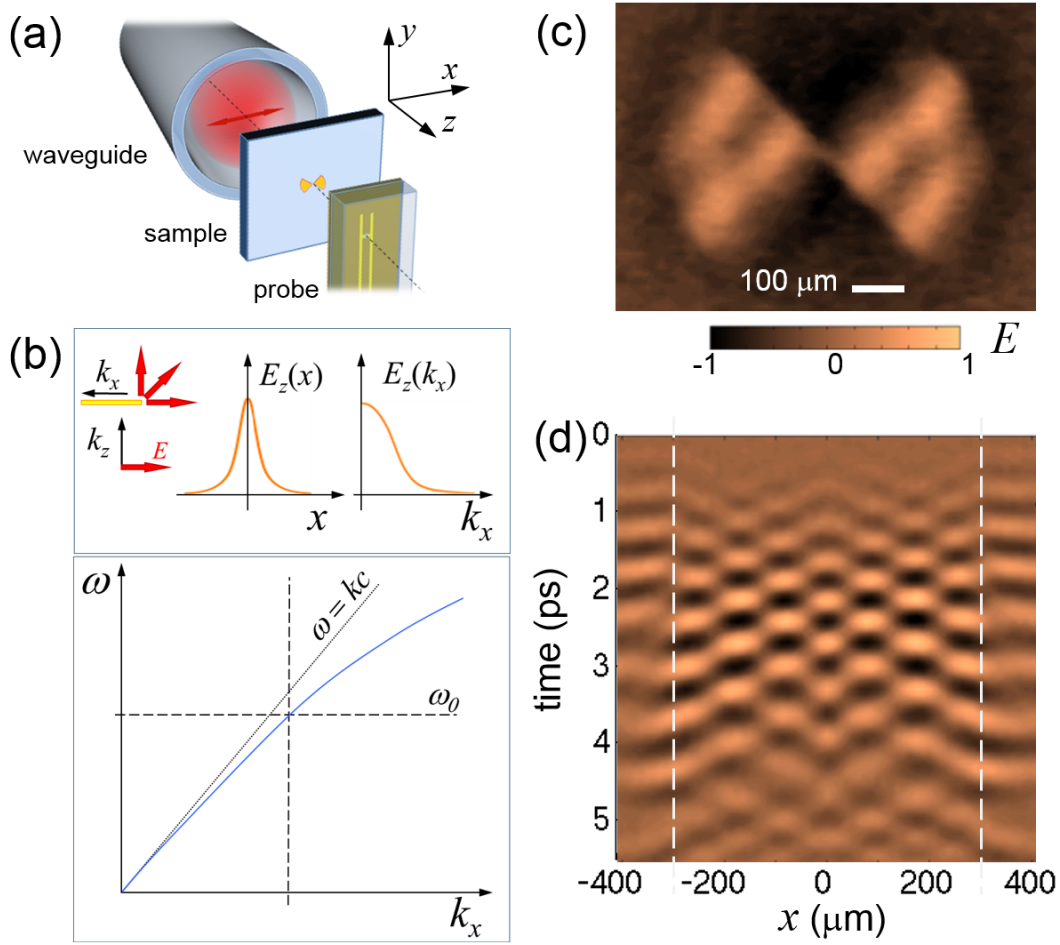


Fig. 1. Near-field microscopy system for probing THz surface plasmon waves. (a) Schematic diagram displaying a hollow THz waveguide, a sample with a metallic pattern placed at the waveguide center, and the integrated THz near-field probe. (b) Mechanism of surface wave excitation at the edges of a metallic pattern. The upper panel shows the spatial distribution and its angular spectrum for the E_z -component induced at the edge. The lower panel shows the dispersion relation for the surface wave (blue line) in a similar k_x range as for the angular spectrum $E_z(k_x)$ in the upper panel. The horizontal dashed line indicates the plane wave dispersion for reference. (c) THz electric field distribution on a metallic bow-tie antenna deposited on a GaAs substrate. The snapshot corresponds to $t = 1.16$ ps. (d) A space-time map of the electric field near the antenna surface during the excitation of the antenna by a THz pulse. Dashed lines mark the location of the bow-tie edges.

spectrum of E_z that matches the transverse component k_x required for launching a surface wave (lower panel of Fig. 1(b)). Therefore, the illumination of a metallic pattern by a plane wave at normal incidence causes excitation of surface waves at the pattern edges.

The process of excitation and propagation of THz surface waves at the edges of a metallic bow-tie antenna was studied in details by *Mueckstein et al.* [27]. Figure 1(c) shows an example of spatial distribution of the electric field on the antenna surface. The antenna surface becomes a resonator for the surface waves that move from one side of the antenna to the other. It is important to note that this THz image shows the electric field distribution on an opaque metallic surface illuminated from the substrate side. Therefore, only the surface waves contribute to the detected field over the antenna area [29].

The surface wave nature of the detected field is verified in its evolution displayed as a space-time map in Fig. 1(d). It shows that the field over the antenna area originates from the edges (marked by the dashed lines). The incident plane wave and the surface waves exhibit distinctive patterns in the space-time map. The phase of the incident plane wave is constant for any position x , thus it is represented by horizontal 'fringes' in the map (outside the region between the dashed lines). The phase of the surface

wave on the other hand changes with x according to the phase velocity relationship and it forms tilted 'fringes' in the map (in the region between the dashed lines).

The space-time map also illustrates that the field pattern on the antenna surface changes over time. At the beginning of excitation, the field is present only near the edges of the antenna. As time elapses the surface waves spread over the entire area of the antenna and a standing wave pattern forms. After the incident pulse passes, the surface waves remain on the antenna surface for several picoseconds, decreasing in amplitude over time and eventually disappearing.

3. Results and discussion

3.1. THz near-field imaging of graphene bow-tie

A bow-tie antenna made of monolayer epitaxial graphene grown on the Si-terminated face of SiC is studied using the same THz near-field microscopy technique (Fig. 1(a)). The multilayer graphene, simultaneously grown on the C-terminated face, is removed by oxygen plasma etching, and the monolayer graphene on the Si-terminated face is identified by Raman spectroscopy and confirmed by transport measurements on samples grown in the same condition. The right-hand side of the bow-tie structure is shown in the optical image in Fig. 2(a). The bow-tie geometry and dimensions are chosen to be the same as for the metallic bow-tie in Fig. 1(c). As in the experimental schematic shown in Fig. 1(a), the bow-tie is illuminated by the THz pulse (Fig. 2(b)) incident from the substrate side.

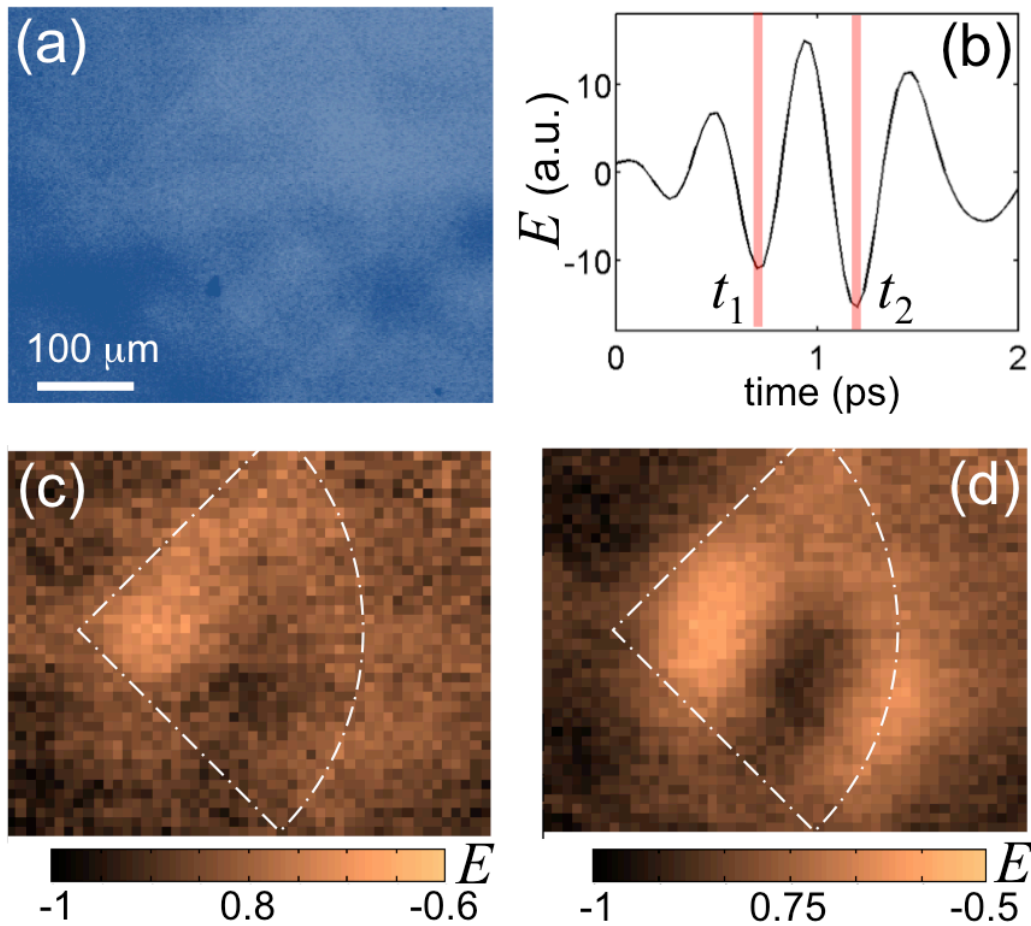


Fig. 2. Graphene bow-tie antenna patterned on SiC substrate. (a) Optical image of the right-hand side of the bow-tie. (b) Waveform of the incident THz pulse, $E_{inc}(t)$. (c,d) THz near-field images of the bow-tie area in (a) captured at $t_1 = 0.67$ ps (c) and $t_2 = 1.13$ ps (d). The color scales are normalized to the field values $E_{inc}(t_1)$ and $E_{inc}(t_2)$, respectively.

Two THz images acquired at two moments, t_1 and t_2 , are shown in Figs. 2(c) and 2(d). In Fig. 2(c), the antenna pattern makes only small impact on the uniform distribution of the electric field. Attenuation of the THz wave by graphene is barely noticeable. The image however shows variation of the field amplitude over the antenna area, similarly to the surface wave interference pattern in Fig. 1(c). This pattern becomes more pronounced in Fig. 2(d) at $t_2 = t_1 + T$, where T is approximately the period of the THz wave, indicating that more energy is converted from the incident plane wave into the surface wave.

The surface wave pattern observed on the graphene bow-tie remarkably replicates the pattern formed on the metallic bow-tie, despite the fact that the metallic layer is opaque for the incident THz wave, whereas the graphene layer is transparent. We note that in the case of graphene, the pattern is superimposed over the incident wave field, which is practically uniform in the xy -plane, while in the metallic bow-tie case, the pattern is formed in the ‘shadow’ area of the antenna, where the incident wave field is zero.

3.2. THz near-field imaging of graphene ribbons

The similarity between the patterns observed on the metallic and graphene bow-ties indicates that the corresponding surface waves are weakly confined as in the case of metallic surfaces [28]. Ribbon arrays on the other hand are predicted to support strongly confined plasmon modes, with the wave-vector several times larger than the free-space wave-vector. To investigate confined plasmon modes we now consider samples with periodic structures on the sub-wavelength scale.

Figure 3 shows a sample, which contains arrays of graphene ribbons oriented parallel and perpendicular to the electric field vector of the incident wave and two areas of continuous graphene, arranged as four quadrants. In this experiment, we use multilayer epitaxial graphene grown on the C-terminated face of SiC. Ellipsometry measurements show that the sample consists of 10 graphene layers. The ribbons in both arrays are $W = 4 \mu\text{m}$ in width and the spacing between the adjacent ribbons is $4 \mu\text{m}$. The frequency of the confined plasmon mode in ribbons is given by [3]

$$\hbar\omega_{pl} = \sqrt{\frac{e^2 E_F}{2\epsilon_0 \epsilon W}}, \quad (1)$$

where \hbar is the reduced Planck’s constant, e is the electron charge, ϵ_0 is the vacuum permittivity, and $\epsilon = (\epsilon_{\text{SiC}} + 1)/2 \approx 5$ is the relative permittivity of epitaxial graphene. Taking $E_F = 215 \text{ meV}$ [23] for the highly doped graphene layers near the interface with SiC, we expect $\omega_{pl} \approx 2.4 \text{ THz}$, while $\omega_{pl} \approx 0.67 \text{ THz}$ for the quasi-neutral top layers where $E_F = 17 \text{ meV}$ [3]. These frequencies fall in the spectral range of our measurement (0.5-2.5 THz).

In our experiment, we find that the detected THz field is noticeably reduced in the areas of all four

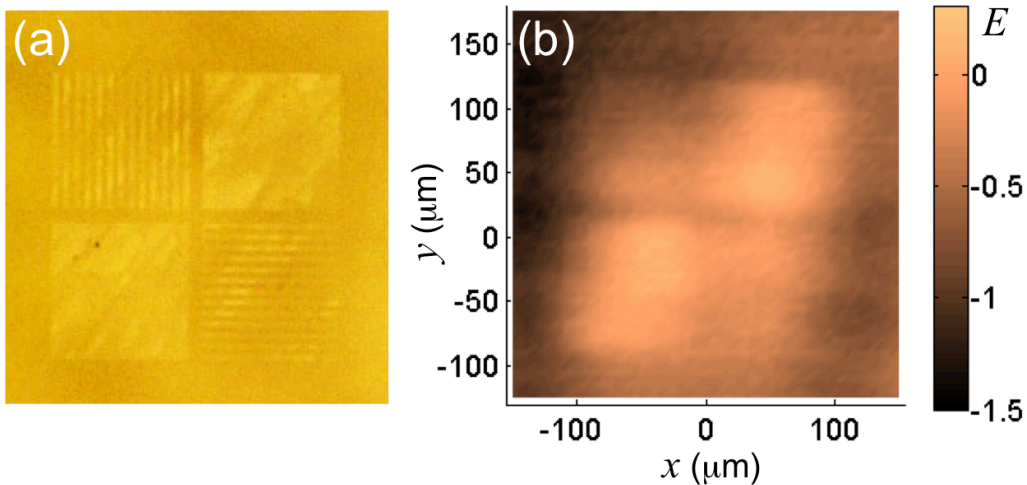


Fig. 3. THz near-field image of multilayer graphene (10-layer) mesas and ribbon arrays: (a) optical image and (b) THz transmission image of the same sample area. The size of the mesas is $100 \mu\text{m} \times 100 \mu\text{m}$; the ribbons are $100 \mu\text{m}$ in length and $4 \mu\text{m}$ in width, and the spacing between the adjacent ribbons is $4 \mu\text{m}$.

quadrants. The continuous mesas show lower transmission compared with the arrays, consistent with the reduced graphene area in the array. It is unlikely that the confined plasmons are excited in these arrays as their response to the incident THz pulse does not show a significant difference for both orientations of the ribbons. Arrays of 200nm-wide graphene ribbons also exhibit no effect of the ribbon orientation in our previous work [21].

A possible explanation for not being able to observe the confined plasmon mode in Fig. 3 is the charge inhomogeneity of the sample, particularly in the highly doped graphene layers close to the interface with SiC. While the near-field probe with a 10 μm aperture does not resolve individual ribbons in Fig. 3, it shows that the transmission coefficient varies considerably within each 100 μm \times 100 μm quadrant. A similar variation of the local transmission properties has also been observed in other multilayer epitaxial graphene samples on SiC [21]. One can attribute this variation to the non-uniform electron density in graphene, caused potentially by the substrate. The electron density affects the dispersion relationship of surface plasmons and thus the non-uniformity is likely to scatter surface plasmon waves.

Arrays of 1 μm -wide graphene ribbons however exhibit a noticeable change in the transmission properties for the two orientations, parallel and perpendicular to the electric field vector. The ribbon arrays were fabricated from multilayer (10-layer) epitaxial graphene grown on the C-terminated face of SiC. The ribbons are 200 μm in length and 1 μm in width, and the spacing between the adjacent ribbons is 1.2 μm . Figure 4 illustrates the orientation dependence by comparing THz space-time maps for three patterns fabricated on the same substrate. The left and right columns display experimental results for the ribbon arrays oriented parallel (left) and perpendicular (right) to the electric field, while the middle column shows the map of continuous graphene (200 μm \times 200 μm square). Although the detected field, $E(x,t)$, is dominated by the incident plane wave (middle row of Fig. 4), there are noticeable changes in the field amplitude in the ribbon regions.

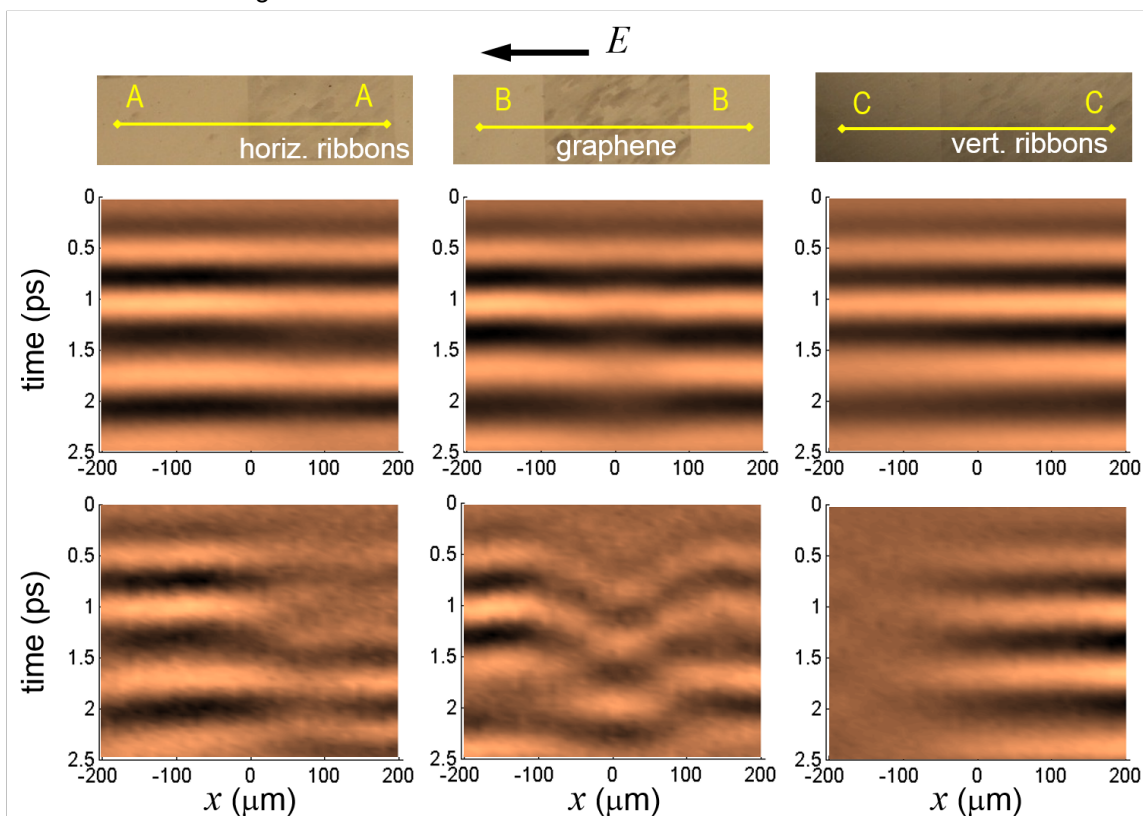


Fig. 4. Near-field THz space-time maps measured for a 200 μm \times 200 μm graphene mesa (middle) and arrays of 1 μm -wide graphene ribbons oriented parallel (left) and perpendicular (right) to the electric field polarization. The space-time maps were obtained within several microns from the sample surface. The top row shows the optical images of the samples; the middle row shows the detected THz field $E(x,t)$; and the bottom row shows $E(x,t) - \alpha \times E_{inc}(t)$, to emphasize the difference in electric field between the graphene pattern and the bare substrate. Here, $\alpha = 0.73$ for horizontal ribbons (left), $\alpha = 0.8$ for graphene mesa (middle), $\alpha = 1$ for vertical ribbons (right), and $E_{inc}(t)$ is a waveform of the reference THz pulse taken on bare SiC substrate without graphene.

To display the changes, we subtract the incident wave from the space-time maps in the bottom row of Fig. 4. For the ribbons parallel to the field, the incident field is scaled by a factor of 0.73 and removed from the detected field, $E(x,t) - 0.73E_{inc}(t)$. The subtraction illustrates that the transmission through the horizontal ribbons is reduced by $\sim 27\%$ compared to the bare SiC substrate. For the ribbons oriented perpendicular to the field, $E(x,t) - E_{inc}(t)$ is plotted. In this case, we find surprisingly that more transmission occurs through the ribbon area (shown as fringe patterns) after subtracting the waveform of the incident THz pulse through the substrate. Quantitative analysis shows that the transmission is increased by $\sim 50\%$ compared to the bare SiC substrate.

In addition, we notice that the subtracted maps in the left and right columns of Fig. 4 show no surface wave patterns in the ribbon array region. Similar background subtraction conducted for the space-time map measured over the graphene mesa (middle column) however reveals the signature of surface waves: the phase of the wave present in the mesa area changes with x , indicating that the surface waves are originated from the edges. The lack of surface waves in graphene ribbon arrays can be caused by several factors: the excitation of surface wave at the end of the ribbon is likely to be less efficient compared to the large-area mesa; the (rough) ribbon edges can also provide additional absorption or scattering for a wave propagating along the ribbon.

The increase in transmission coefficient for the area with ribbons oriented perpendicular to the electric field compared to the bare SiC substrate requires a more detailed consideration. One possible interpretation is that it is due to the impedance matching provided by the graphene ribbon array. The THz wave incident on the SiC-air interface experiences significant partial reflection because of the large refractive index contrast ($n_{SiC} \approx 3.0$). The reflection coefficient can be reduced if graphene acts as an impedance matching layer. For example, it was reported recently that a continuous graphene layer can exhibit complete elimination of reflection from the quartz-air and silicon-air interfaces [30]. In the case of the ribbon array, the impedance matching can occur if the reflected waves from the SiC-air (between adjacent ribbons) and SiC-graphene-air interface have opposite polarities, producing a destructive interference and therefore minimizing the reflected wave amplitude. This effect should not be frequency selective, but dependent on the filling ratio of the array and the Fermi energy. The latter affects the conductivity of graphene. The impedance matching explanation is consistent with the lack of the surface waves originating from the ribbon array edges. Further finite-element simulations are needed to explain why the orientation dependent effect is absent in the $4\mu\text{m}$ -wide and 200nm -wide ribbon arrays with a similar graphene filling ratio ($\sim 50\%$).

An alternative interpretation for the enhanced transmission through the ribbons oriented perpendicular to the electric field is the excitation of the confined surface plasmons in the ribbon array. In this case, oscillating and possibly enhanced field is expected near the surface. Our experiment however shows no phase shift in the detected field and no induced oscillations following the incident pulse. The response of the ribbons is expected to be dominated by the highly doped layers of graphene close to the interface with SiC and $\omega_{pl} \approx 4.8$ THz from Eq. (1), beyond the spectral range of our technique (0.5-2.5 THz). It is worth mentioning that $\omega_{pl} \approx 1.3$ THz for the high-mobility quasi-neutral top layers of graphene in our samples, and it is centered in our spectral range. Further experimental work is needed to understand the effect of the confined plasmons in the quasi-neutral graphene top layers.

4. Conclusions

We have performed THz near-field microscopy study of epitaxial graphene structures (bow-ties, mesas, and ribbons) and observed surface plasmon waves excited at the edges of graphene structures (similar to metallic edges). Near-field images show that the THz absorption of graphene varies on a scale smaller than the wavelength and the Fresnel reflection at the SiC substrate surface is modified by the presence of graphene ribbons, leading to either reduced or enhanced transmission of THz waves depending on the orientation of the ribbons with respect to the electric field and the ribbon width. The observations illustrate intriguing properties of graphene, which hold promise for new applications in THz spectroscopy, sensing, imaging, and communications. They also illustrate complexity of graphene plasmonic responses.

Acknowledgments

This work was supported by the Royal Society [Grant No. UF080745] and performed at UCL and at the Center for Integrated Nanotechnologies, an Office of Science User Facility operated for the U.S.

Department of Energy (DOE) Office of Science by SNL [Contract No. DE-AC04-94AL85000]. Epitaxial graphene growth and device fabrication are carried out at GaTech, supported by the NSF [DMR-0820382] and the DOE Office of Basic Energy Sciences through a contract with SNL. The work at SNL was supported by a Laboratory Directed Research and Development project. Sandia National Laboratories is a multi-program laboratory managed and operated by Sandia Corporation, a wholly owned subsidiary of Lockheed Martin Corporation, for the U.S. Department of Energy's National Nuclear Security Administration under contract DE-AC04-94AL85000.

References

1. A. N. Grigorenko, M. Polini, and K. S. Novoselov, *Nat Photon* 6 (2012) 749-758.
2. M. Jablan, H. Buljan, and M. Soljačić, *Physical Review B* 80 (2009) 245435.
3. J. M. Pomirol, W. Yu, X. Chen, C. Berger, W. A. de Heer, M. L. Smith, T. Ohta, W. Pan, M. O. Goerbig, D. Smirnov, and Z. Jiang, *Physical Review Letters* 110 (2013) 246803.
4. L. Ju, B. Geng, J. Horng, C. Girit, M. Martin, Z. Hao, H. A. Bechtel, X. Liang, A. Zettl, Y. R. Shen, and F. Wang, *Nat Nano* 6 (2011) 630-634.
5. H. Yan, X. Li, B. Chandra, G. Tulevski, Y. Wu, M. Freitag, W. Zhu, P. Avouris, and F. Xia, *Nat Nano* 7 (2012) 330-334.
6. W. Gao, G. Shi, Z. Jin, J. Shu, Q. Zhang, R. Vajtai, P. M. Ajayan, J. Kono, and Q. Xu, *Nano Letters* 13 (2013) 3698-3702.
7. I. Crassee, M. Orlita, M. Potemski, A. L. Walter, M. Ostler, T. Seyller, I. Gaponenko, J. Chen, and A. B. Kuzmenko, *Nano Letters* 12 (2012) 2470-2474.
8. J. H. Strait, P. Nene, W.-M. Chan, C. Manolatou, S. Tiwari, F. Rana, J. W. Kevek, and P. L. McEuen, *Physical Review B* 87 (2013) 241410.
9. H. Yan, T. Low, W. Zhu, Y. Wu, M. Freitag, X. Li, F. Guinea, P. Avouris, and F. Xia, *Nat Photon* 7 (2013) 394-399.
10. V. W. Brar, M. S. Jang, M. Sherrott, S. Kim, J. J. Lopez, L. B. Kim, M. Choi, and H. Atwater, *Nano Letters* 14 (2014) 3876-3880.
11. H. Yan, Z. Li, X. Li, W. Zhu, P. Avouris, and F. Xia, *Nano Letters* 12 (2012) 3766-3771.
12. J. Chen, M. Badioli, P. Alonso-Gonzalez, S. Thongrattanasiri, F. Huth, J. Osmond, M. Spasenovic, A. Centeno, A. Pesquera, P. Godignon, A. Zurutuza Elorza, N. Camara, F. J. G. de Abajo, R. Hillenbrand, and F. H. L. Koppens, *Nature* 487 (2012) 77-81.
13. Z. Fei, A. S. Rodin, G. O. Andreev, W. Bao, A. S. McLeod, M. Wagner, L. M. Zhang, Z. Zhao, M. Thiemens, G. Dominguez, M. M. Fogler, A. H. C. Neto, C. N. Lau, F. Keilmann, and D. N. Basov, *Nature* 487 (2012) 82-85.
14. F. Keilmann and S. Amarie, *J Infrared Milli Terahz Waves* 33 (2012) 479-484.
15. F. Bonaccorso, Z. Sun, T. Hasan, and A. C. Ferrari, *Nat Photon* 4 (2010) 611-622.
16. F. Rana, *Nanotechnology*, *IEEE Transactions on* 7 (2008) 91-99.
17. V. Ryzhii, A. A. Dubinov, T. Otsuji, V. Mitin, and M. S. Shur, *Journal of Applied Physics* 107 (2010) 054505.
18. H. Choi, F. Borondics, D. A. Siegel, S. Y. Zhou, M. C. Martin, A. Lanzara, and R. A. Kaindl, *Applied Physics Letters* 94 (2009) 172102.
19. M. J. Paul, J. L. Tomaino, J. W. Kevek, T. DeBorde, Z. J. Thompson, E. D. Minot, and Y.-S. Lee, *Applied Physics Letters* 101 (2012) 091109.
20. J. D. Buron, D. H. Petersen, P. Bøggild, D. G. Cooke, M. Hilke, J. Sun, E. Whiteway, P. F. Nielsen, O. Hansen, A. Yurgens, and P. U. Jepsen, *Nano Letters* 12 (2012) 5074-5081.
21. O. Mitrofanov, W. Yu, R. J. Thompson, Y. Jiang, I. Brener, W. Pan, C. Berger, W. A. de Heer, and Z. Jiang, *Applied Physics Letters* 103 (2013) 111105.
22. W. A. de Heer, C. Berger, M. Ruan, M. Sprinkle, X. Li, Y. Hu, B. Zhang, J. Hankinson, and E. Conrad, *Proceedings of the National Academy of Sciences* 108 (2011) 16900-16905.
23. C. Berger, Z. Song, X. Li, X. Wu, N. Brown, C. Naud, D. Mayou, T. Li, J. Hass, A. N. Marchenkov, E. H. Conrad, P. N. First, and W. A. de Heer, *Science* 312 (2006) 1191-1196.
24. J. Hass, F. Varchon, J. E. Millán-Otoya, M. Sprinkle, N. Sharma, W. A. de Heer, C. Berger, P. N. First, L. Magaud, and E. H. Conrad, *Physical Review Letters* 100 (2008) 125504.
25. M. L. Sadowski, G. Martinez, M. Potemski, C. Berger, and W. A. de Heer, *Physical Review Letters* 97 (2006) 266405.

26. O. Mitrofanov, M. Lee, J. W. P. Hsu, I. Brener, R. Harel, J. F. Federici, J. D. Wynn, L. N. Pfeiffer, and K. W. West, Selected Topics in Quantum Electronics, IEEE Journal of 7 (2001) 600-607.
27. R. Mueckstein, C. Graham, C. Renaud, A. Seeds, J. Harrington, and O. Mitrofanov, J Infrared Milli Terahz Waves 32 (2011) 1031-1042.
28. M. Natrella, O. Mitrofanov, R. Mueckstein, C. Graham, C. C. Renaud, and A. J. Seeds, Opt. Express 20 (2012) 16023-16031.
29. O. Mitrofanov, C. C. Renaud, and A. J. Seeds, Opt. Express 20 (2012) 6197-6202.
30. Y. Zhou, X. Xu, F. Hu, X. Zheng, W. Li, P. Zhao, J. Bai, and Z. Ren, Applied Physics Letters 104 (2014) 051106.